Global Cities under Multiple Climate Hazards

Rita Nogherotto
r.nogherotto@isac.cnr.it

Institute of Atmospheric Sciences and Climate (CNR-ISAC, Italy) https://orcid.org/0000-0003-1718-542X

Natalia Zazulie
The Abdus Salam International Centre for Theoretical Physics (ICTP, Italy)

Roshanka Ranasinghe
IHE Delft https://orcid.org/0000-0001-6234-2063

Trang Duong
IHE Delft Institute for Water Education

Felix Creutzig
Potsdam Institute for Climate Impact Research

Francesca Raffaele
National Institute of Oceanography and Applied Geophysics (OGS, Italy)

Erika Coppola
Abdus Salam International Centre for Theoretical Physics https://orcid.org/0000-0001-6944-5815

Article

Keywords: climate hazards, mitigation, adaptation, time of emergence, coastal flooding, urban

Posted Date: March 17th, 2026

DOI: https://doi.org/10.21203/rs.3.rs-9095347/v1

Additional Declarations: There is **NO** Competing Interest.

Abstract

Cities concentrate population, infrastructure, and economic assets, yet climate risk studies are still largely conducted at regional or national scales. We provide the first global city-scale assessment of climate change emergence and coastal flood exposure across ~11,000 urban areas, distinguishing four city typologies. Using the policy-relevant CORDEX-CORE ensemble of high-resolution regional models, we analyse projected climatic hazards. We show that many cities experience stronger changes than the surrounding regional average and we quantify when projected climate signals emerge from historical variability under high- and low- emission scenarios. Heat extremes have already emerged in most cities, while by 2050 all analyzed hazards will emerge everywhere. Mitigation delays emergence, with heterogeneous benefits across city typologies and continents. Coastal flood exposure is strongly shaped by socio-economic gradients, and flood protection reduces wealth-dependent disparities. These findings highlight the need to move beyond a megacity-centric view of climate risk and include small and intermediate coastal cities in global adaptation planning.

Introduction

Urban areas are increasingly recognized as critical focal points of climate risk, where the interaction between anthropogenic activities, dense populations, and modified land surfaces exacerbates the impacts of global climate change. According to the Sixth Assessment Report (AR6) of Intergovernmental Panel on Climate Change Sixth Assessment Report (IPCC)[1], urban exposure to climate hazards is increasing due to both global-scale climatic trends and the local amplification of extremes through urbanisation processes. There is very high confidence that urban environments experience enhanced local warming as a consequence of the urban heat island effect, leading to an intensification of heatwaves, and medium confidence of altered precipitation regimes that affect both mean and extreme rainfall. There is high confidence that these changes contribute to stronger runoff events and flash flooding [2]. Furthermore, drought conditions are projected to intensify in many areas due to rising temperatures and changes in precipitation patterns, especially where urban water demand and changes to the land surface exacerbate hydrological stress [3–5]. Particularly, in cities situated at the urban-wildland interface, drying trends, increased temperatures, and modifications in atmospheric circulation can also favor conditions favorable to wildfire activity. By combining the effects of temperature, humidity, wind, and fuel dryness, compound indicators that integrate multiple climatic drivers, such as the Fire Weather Index (FWI) and heat-stress metrics (e.g. NOAA HI), offer a helpful framework to evaluate these interacting hazards [6,7]. These compound indicators show how risks to urban populations, ecosystems, and infrastructure can be increased by concurrent changes in several climate variables.

Urbanized and densely populated areas in coastal cities are particularly vulnerable to flooding, as sea-level rise and storm surges combine with extreme precipitation to produce compound flooding hazards. The frequency of extreme sea-level events has already increased substantially, and this trend is projected to accelerate throughout the 21st century [8]. Consequently, virtually all urban areas face heightened risks to human health, infrastructure, and economic systems [9]. Despite the clear relevance of urban land-atmosphere interactions for climate risk assessments, most large-scale studies to date have relied on global climate model (GCM) ensembles. For instance, Guerreiro et al. (2018)[10] analysed projections from the Coupled Model Intercomparison Project Phase 5 (*CMIP5*) to assess future heatwave characteristics across European cities. However, GCMs typically operate at spatial resolutions of approximately 100 km, which are insufficient to capture the fine-scale variability and feedback associated with urban land surfaces. As a result, urban-rural contrasts and local amplification processes are only coarsely represented in these studies.

To resolve these local-scale processes, dynamical downscaling using regional climate models (RCMs) is commonly employed. Within the CORDEX framework (Coordinated Regional Climate Downscaling Experiment [11]), global CMIP models are downscaled to regional domains, providing climate projections at grid spacings of approximately 0.22° (~25 km) in CORDEX-CORE (Coordinated Output for Regional Evaluations) and 0.11° (~12 km) in EURO-CORDEX. These simulations improve the representation of regional extremes and land-atmosphere interactions compared to GCMs [12–18]. Such high-resolution approaches have been applied extensively to examine the urban climate of individual cities or limited regions due to computational demand (e.g., [19–24]). However, large-scale or ensemble-based assessments covering multiple urban areas remain comparatively scarce, with only a few examples addressing multi-city analyses or cross-model comparisons (e.g., [25–27]).

Some recent studies have incorporated explicit urban parameterizations, such as urban canopy models (UCMs), within regional simulations, substantially improving the representation of urban heat island characteristics and urban–rural contrasts. For example, Langendijk et al. (2025) [28] analysed global megacities using CORDEX-CORE simulations with urban representations, while Zazulie et al. (2026)[29] investigated extreme climate indices for 40 European cities using EURO-CORDEX simulations including urban parameterizations. However, in CMIP5-driven CORDEX simulations, the urban fraction or urban mask was not a mandatory output variable. Consequently, urban-focused analyses have been restricted to a relatively small subset of simulations and cities for which explicit urban information was available. This has resulted in spatially limited assessments, typically covering around 40 cities, and leaving cities in large portions of the world unexplored.

In the absence of a globally consistent dataset with explicit urban parameterizations, and while awaiting the next generation of CORDEX simulations driven by CMIP6 models, there is a need for intermediate approaches that can provide a first-order, globally consistent representation of how climate extremes affect cities worldwide.

To overcome this limitation and to deliver a first global overview of climate impacts on cities using the data currently available, the present study employs the full ensemble of CMIP5-driven CORDEX-CORE and EURO-CORDEX simulations at 0.22° and 0.11° resolution, respectively. Rather than relying on model-based urban masks, which are not implemented consistently across regions or for cities of all sizes, we combine these regional climate projections with harmonised spatial information on urban extents from the Global Human Settlement Urban Centre Database (GHS-UCDB, Globe R2024A [30]). Specifically, urban polygons from GHS-UCDB are used to spatially extract and aggregate climate information from the CORDEX simulations over the locations corresponding to each city. This approach does not explicitly represent urban canopy processes within the climate models, but it ensures methodological consistency across continents and city sizes. It therefore represents an intermediate and pragmatic compromise, enabling a globally comparable

assessment of climate extremes affecting urban areas under a common framework.
Using this framework, we analyse a suite of extreme indices derived from near-surface air temperature, maximum and minimum temperature (*tas, tasmax, tasmin*), precipitation (*pr*), relative humidity (*hurs*) and surface wind (*sfcWind*), including compound indicators such as the NOAA Heat Index [31] and the Fire Weather Index (FWI)[32]. To extend the assessment beyond atmospheric hazards, we further integrate two complementary global coastal flood hazard datasets representing exposure with and without coastal protection measures. Through this multi-hazard approach, our study provides a globally consistent assessment of projected climate extremes in urban areas, quantifying the timing of emergence of heat- and precipitation-related hazards under both RCP8.5 and RCP2.6, and assessing coastal flood exposure under a high-end RCP8.5 scenario. Coastal flood projections under RCP2.6 were not available in the underlying dataset; while simulations for RCP4.5 exist, they produce results broadly comparable (not shown) to those obtained under RCP8.5 and are therefore not discussed separately.This first-order global overview lays the groundwork for future analyses based on fully coupled urban-climate simulations.

Results

Extreme indices over cities

Cities in this study are classified according to the global urban typology developed by Montfort et al. (2026)[33], which encompasses approximately 11,000 cities worldwide with at least 50,000 inhabitants. The dataset identifies four city types capturing major dimensions of urban development and climate relevance: Type 1: “Development First”, characterized by low emissions and urgent development challenges; Type 2: “Urban Planning First”, representing rapidly growing cities supported by robust infrastructure and governance structures; Type 3: “Mitigation First”, including high-emission cities with substantial mitigation potential; and Type 4: “Megacities”, comprising globally significant metropolitan areas facing complex, cross-cutting socio-environmental pressures (see Methods). The spatial distribution of cities analysed in this study is shown in Fig. 1.

To better characterise how climate change signals manifest at the city scale, we analysed how changes simulated for individual cities compared with the corresponding AR6 regional mean signal. Cities are unevenly distributed within regions and often located in climatically distinct sub-areas (e.g. coastal zones, lowlands or orographic margins), and so their local climate response may differ in magnitude from the regional average. Using the Montfort et al (2026)[33] global dataset and the full ensemble of CORDEX-CORE simulations, we quantified, for each AR6 region and climate index (Table 1), including temperature extremes (TN90p, TX90p), heat stress (HI41), energy-related degree days (HeatDD, CoolDD), precipitation extremes (CDD, RX1DAY), and fire weather conditions (FWI), the percentage of cities (P) in which the projected change (Δcity,i) across models (N) exceeds the regional mean change (Δregion,i), while retaining the sign of the regional signal using equation (1). The change was computed as the difference between the far-future period (2070–2100) and the historical reference period (1980–2010) :

$$P = \frac{100}{N} \sum_{i=1}^{N} \quad [sign(\Delta_{region,i}) \cdot (\Delta_{city,i} - \Delta_{region,i}) \ \ ] \quad > 0 \qquad [1]$$

We show these percentages in Fig. 2: background colours indicate the sign of the regional mean change, while dot size and shading represent the proportion of cities for which the change exceeds the regional mean in the same direction. The dot patterns reveal substantial intra-regional heterogeneity. For temperature extremes (TX90p and TN90p), a large fraction of cities, often exceeding 50% and in several regions approaching 75-100%, experience stronger changes than the regional mean, particularly in parts of Central and South America, Africa, and Asia. The amplification is even more pronounced for HI41 in several tropical and subtropical regions, where the majority of cities show changes larger than the regional average. For precipitation-related indices (RX1DAY and CDD), the spatial patterns are more variable. Some regions exhibit high percentages of cities with amplified changes, while others show a more balanced distribution, suggesting that local-scale factors and spatial heterogeneity play a stronger role. Fire Weather Index (FWI) displays widespread regional increases, with many regions, especially in Northern and Central South America and parts of Asia, showing a high proportion of cities with stronger-than-regional amplification. Overall, this analysis highlights that regional mean values can mask significant sub-regional variability. In many AR6 regions and across multiple indices, a majority of cities exhibit changes that exceed the corresponding regional average, underscoring the importance of city-level assessments in complementing regional-scale climate projections.

ToE across types and regions

In climate science, the Time of Emergence (ToE) refers to the moment when the climate-change signal of a given variable exceeds the range of natural variability, making the influence of anthropogenic forcing clearly detectable (see Methods). Analysing ToE across different hazard types and city typologies allows us to disentangle whether the timing of climate signal detection is primarily controlled by the physical characteristics of each hazard or modulated by regional and urban context.

In Fig. 3 the upper panel (a) shows when each hazard emerges across cities, while the lower panels illustrate, for each city typology, which hazards dominate among those emerging before 2025 and before 2050. The timing of emergence varies substantially across hazards. Temperature-based extremes (TX90p and TN90p) show universally very early emergence, with 100% of cities exceeding natural variability before 2025. Heat-related compound indices (HI41) and drought/fire-related metrics (CDD and FWI) also emerge predominantly before mid-century, with 77%–90% of cities crossing the threshold before 2025 and only a small fraction emerging after 2035. In contrast, precipitation extremes (RX1DAY) display later emergence: only 20% of cities emerge before 2025, while 38% do so between 2035 and 2050 and 13% after 2050. Energy demand indicators show differentiated behaviour: Cooling Degree Days (CoolDD) emerge almost universally before 2025 (99%), reflecting increasing cooling demand, whereas Heating Degree Days (HeatDD) exhibit a more gradual signal, with 25% of cities emerging after 2035 and 17% after 2050. The lower panel (b) reveals that differences across city typologies (Megacities, Development-first, Mitigation-first, and Urban-planning-first) are secondary compared to hazard-specific physical characteristics. Before 2025, temperature extremes dominate across all typologies, consistently reaching 100% emergence. By 2050, nearly all hazards have emerged in most cities, though RX1DAY and, in some typologies, HI41 retain lower shares compared to thermodynamic indicators. Notably, mitigation-first cities show slightly delayed emergence for some hydro-climatic hazards (e.g., HI41 and RX1DAY), whereas development-first and megacities display broader early emergence across compound and fire-related indices. Overall, the figure highlights that the timing of emergence is primarily hazard-driven rather than city-typology-driven. Thermodynamic warming signals (TX90p, TN90p, CoolDD) emerge earliest and most robustly, followed by heat stress and fire weather metrics, while precipitation extremes and cold-related declines exhibit greater variability and later emergence. This sequential emergence pattern has implications for adaptation planning, suggesting that cities worldwide are already locked into early and robust warming-related impacts, with hydro-climatic extremes becoming increasingly dominant toward mid-century.

Figure 4 disaggregates the timing of hazard emergence by continent, highlighting regional contrasts in the sequencing of climate hazards. A clear and consistent pattern emerges across all regions: temperature-based extremes (TX90p and TN90p) display universal early emergence, with 100% of cities exceeding baseline variability before 2025 in every continent. This confirms the robustness and spatial coherence of the warming signal across diverse climatic contexts. Cooling Degree Days (CoolDD) also show near-universal early emergence, reflecting increasing cooling demand across climatic zones. Greater regional differentiation appears for hydro-climatic and compound hazards. For RX1DAY, early emergence before 2025 remains limited in most continents (typically below 50%), with Europe showing particularly low early emergence (6%). However, by 2050, the vast majority of cities in all continents have crossed the emergence threshold, indicating a delayed but widespread and fast intensification of extreme precipitation. CDD and FWI display strong early signals in Africa, Asia, and parts of the Americas, where more than 80%–90% of cities show emergence before 2025. Australasia stands out for comparatively lower early emergence of CDD (48%) and HI41 (55%), although both indices approach near-universal emergence by 2050. Europe exhibits a distinct profile, with very early emergence of FWI (98%) but more moderate early emergence of HI41 (19%) and RX1DAY (6%), suggesting stronger regional modulation of compound heat and precipitation extremes. Overall, the continental breakdown reinforces that while warming-related hazards emerge early and consistently across the globe, precipitation and compound heat indicators exhibit stronger regional modulation in their timing. By 2050, however, most hazards are projected to emerge in the majority of cities across all continents, indicating a progressive convergence of climate risk profiles despite differing initial trajectories.

Figure 5 illustrates the effect of mitigation on the Time of Emergence, expressed as the difference in years between the RCP2.6 and RCP8.5 ($\Delta ToE = ToE_{RCP2.6} - ToE_{RCP8.5}$). Positive values indicate a delayed emergence under the low-emission scenario relative to the high-emission pathway. Results are shown as mean across cities, stratified by city typology (a) and by continent (b).

Across hazards, mitigation systematically delays the emergence of climate hazards, but the magnitude of this delay varies strongly by hazard, city typology, and continent. Percentile-based temperature extremes (TX90p, TN90p) show only limited delays (typically <2 years), indicating that their emergence is already largely locked-in across scenarios. In contrast, substantially larger delays are found for compound and cumulative heat indicators such as HeatDD and HI41, for which mitigation can postpone emergence by more than 5-10 years in several regions and city typologies.

Hydrological and wildfire hazards (CDD, RX1DAY, FWI) exhibit intermediate and highly heterogeneous responses, with median delays ranging from 2 to more than 10 years depending on the region. These delays are generally larger in North America, South and Central America, and parts of Europe, and smaller in Africa, Australasia and Asia, consistent with the earlier emergence patterns shown in the previous figures. Differences among city typologies are comparatively smaller than regional differences, suggesting that continental-scale climate dynamics appear to play a larger role in determining the mitigation benefit than differences in urban development pathways.

Urban coastal flooding

In addition to climate extremes over land, coastal flooding represents one of the most direct and economically consequential pathways through which climate change affects urban areas. Rising mean sea level, compounded by storm surge, tides, and wave setup, is projected to substantially increase the frequency and magnitude of extreme coastal water levels during the 21st century[34,35]. Beyond the intensification of extreme sea levels, recent work emphasizes that the exposure of the built environment itself represents a critical and growing dimension of coastal climate risk[36], particularly in rapidly urbanizing regions of the Global South[37]. Given the high concentration of population, infrastructure, and economic assets in low-elevation coastal zones, understanding the spatial distribution of flood exposure across coastal cities is critical for assessing future urban climate risk and inequalities in vulnerability. Coastal flood risk is shaped not only by physical drivers, such as relative sea-level rise and extreme sea levels, but also by socio-economic factors, including the spatial configuration of urban areas and the presence (or absence) of coastal protection. In this section, we therefore analyse projected coastal flood exposure across a globally consistent sample of coastal cities, explicitly contrasting scenarios with and without flood protection. This allows us to disentangle the extent to which future coastal flood exposure is driven by physical hazard intensification versus differences in adaptation capacity and protection standards. The coastal flooding analysis relies on two global hazard datasets representing contrasting assumptions about coastal protection: a no-protection scenario (NO_PROT [35]), which assumes the absence of coastal defence measures, and a protection scenario (PROT [38]), which accounts for existing coastal protection standards and their capacity to reduce flood impacts (see Methods). These studies provide spatially explicit projections of coastal flooding under future sea-level rise scenarios, providing the basis for the flood hazard datasets used here.

The analysis focuses on a global set of approximately 1,000 coastal cities from Montfort et al (2026)[33], covered in the coastal flood impact dataset of Kirezci et al. (2020)[35] and Tiggeloven et al. (2020)[38]. Urban extents for each city were delineated using the GHS_UCDB_THEME_CLIMATE_GLOBE_R2024A[30] dataset , which supplies consistent satellite-derived polygons of urban centres and is used to define the spatial footprint over which flood exposure is evaluated. For each city and scenario, the percentage of flooded urban area was computed as the fraction of urban polygon pixels intersecting flood depths greater than zero. This metric provides a consistent basis for comparing flood exposure across cities, continents, and protection scenarios. Figure 6 shows the relationship between urban GDP in 2020 (source: 30) and the projected percentage of flooded urban areas in 2100 under the RCP8.5 scenario, for events with a 100-year return period (RP), stratified by continent. For each region, two sets of points are displayed, corresponding to simulations without flood protection (NO_PROT) and with protection (PROT). For both cases, the association between GDP and the percentage of flooded urban areas is quantified using Spearman's rank correlation coefficient (ρ). Spearman's ρ ranges between −1 and +1, where negative values indicate an inverse relationship and positive values indicate a direct association between variables, while values closer to zero indicate weaker relationships. The corresponding p-values represent the probability of obtaining a correlation at least as extreme as the observed one under the null hypothesis of no association, and are reported to assess statistical significance; correlations with $p < 0.05$ are considered statistically significant.

Linear trend lines are shown to aid visual interpretation. Correlation coefficients and associated p-values are reported in each panel, based on city-level data aggregated by continent. Across all continents, a negative relationship emerges between urban GDP and the fraction of flooded urban areas, particularly in the absence of flood protection. Under the NO_PROT scenario, this relationship is statistically significant in all regions, with moderate correlations in Asia ($\rho = -0.30$, $p = 2.8\times10^{-16}$) and Europe ($\rho = -0.27$, $p = 8.4\times10^{-4}$), and much stronger gradients in Africa ($\rho = -0.60$, $p = 1.4\times10^{-11}$) and Central & South America ($\rho = -0.55$, $p = 3.5\times10^{-7}$). North America also exhibits a significant negative association ($\rho = -0.35$, $p = 7.0\times10^{-3}$), while Australasia shows a moderate but significant correlation ($\rho = -0.50$, $p = 8.6\times10^{-3}$), although based on a smaller sample. In contrast, under the PROT scenario, correlations systematically weaken and often lose statistical significance, with non-significant relationships in Africa ($\rho = -0.15$, $p = 0.13$), Australasia ($\rho = -0.05$, $p = 0.79$), North America ($\rho = -0.16$, $p = 0.24$), and Central & South America ($\rho = -0.06$, $p = 0.60$), while remaining modest but significant in Asia ($\rho = -0.26$, $p = 2.4\times10^{-12}$) and Europe ($\rho = -0.22$, $p = 7.5\times10^{-3}$). Overall, these results suggest that, in the absence of protection, urban flood exposure would be strongly structured by socio-economic gradients, whereas maintaining present levels of flood protection substantially reduces GDP-dependent disparities, effectively flattening the relationship between wealth and flood impacts across most regions.
Figure 7 further refines the analysis by shifting from a continental aggregation to a classification by urban development typology, revealing important differences in how economic capacity relates to flood exposure.

For Megacities, no statistically significant relationship emerges between urban GDP and the percentage of flooded area, either in the absence of protection (NO_PROT: $\rho = +0.04$, $p = 0.82$) or with protection (PROT: $\rho = -0.02$, $p = 0.90$). This lack of correlation is likely explained by the fact that megacities are, by definition, characterized by uniformly high GDP levels, resulting in a limited economic gradient within this group. As a consequence, variations in flood exposure among megacities are more plausibly driven by geographic and physical factors, such as coastal setting, deltaic location, or subsidence, rather than differences in economic capacity. In contrast, cities classified as "Development first" exhibit a clear and robust negative relationship between GDP and flooded urban area in the NO_PROT scenario ($\rho = -0.30$, $p = 4.3\times10^{-10}$), which remains statistically significant but weaker when protection is included ($\rho = -0.17$, $p = 7.6\times10^{-4}$). This suggests that, within this typology, wealthier cities will experience lower relative flood exposure, and that coastal protection reduces both absolute flood impacts and their dependence on economic disparities. A similar but more pronounced pattern is observed for "Mitigation first" cities, where the negative correlation is particularly strong in the absence of protection ($\rho = -0.37$, $p = 4.3\times10^{-13}$) and becomes weak and only marginally significant under protection ($\rho = -0.10$, $p = 7.3\times10^{-2}$). This indicates that, in mitigation-oriented urban systems, economic capacity strongly conditions flood exposure when no defenses are present, whereas protection measures substantially reduce these differences. Finally, for cities categorized as "Urban planning first", correlations are weak and not statistically significant in both scenarios (NO_PROT: $\rho = -0.08$, $p = 0.18$; PROT: $\rho = -0.04$, $p = 0.47$), implying that flood exposure in these cities is largely decoupled from GDP levels. This likely reflects the dominant role of spatial planning, land-use regulation, and urban form in shaping flood risk, independently of economic size.
Overall, the analysis highlights that the relationship between economic wealth and flood exposure is highly contingent on urban development pathways: it is strong in "Development first" and "Mitigation first" cities without protection, weak or absent in "Megacities" due to their uniformly high GDP, and largely neutralized by effective coastal protection across all typologies. Building on the previous analysis of the GDP-exposure relationship, Fig. 8 provides a complementary perspective by examining the full distribution of projected flooded urban areas across continents and time horizons. The figure shows the percentage of flooded urban areas under RCP8.5 for 100-year return period events (RP100), comparing scenarios without protection (NO_PROT) and with protection (PROT), and overlaying projections for 2030, 2050, and 2100. The upper panel (a) includes small and intermediate coastal cities, following the classification of Cattaneo et al 2024[39], with populations between 50.000 and 1 million inhabitants.

The lower panel (b) focuses exclusively on large coastal cities (>1 million inhabitants, 167 cities in total). Across all continents, the NO_PROT scenario exhibits a clear upward shift in both median and upper-tail flood exposure over time, with particularly pronounced increases by 2100 in Europe, Asia, and Africa. The distributions are right-skewed, indicating that while many cities experience moderate impacts, a subset faces very high flooded area fractions. In contrast, the PROT scenario substantially compresses the distributions toward near-zero exposure in most regions and time slices, markedly reducing both median impacts and extreme outliers. When focusing on large cities (>1M inhabitants), overall flooded fractions are generally lower than those observed for small and intermediate coastal cities, although regional contrasts persist. Asia remains the continent with the highest projected exposure even among large cities, whereas Europe and North America show relatively limited impacts under protection scenarios. The strong reduction observed under PROT across all continents reinforces the earlier finding that coastal protection plays a decisive role in moderating exposure disparities, effectively dampening both temporal escalation and regional inequalities in projected flood impacts. Differences across the time horizons considered (2030, 2050, and 2100) remain relatively limited in most regions, suggesting that the presence/absence of coastal protection exerts a stronger influence on projected exposure than the temporal progression itself within the RCP8.5 scenario. A noteworthy pattern emerging from Fig. 8 is that the highest fractions of flooded urban areas are predominantly associated with smaller and intermediate cities. In contrast, large metropolitan areas (> 1 million inhabitants) tend to exhibit comparatively lower flooded fractions. This suggests that extreme proportional exposure is not primarily concentrated in the largest urban economies, but rather in smaller coastal cities, which may be more spatially constrained, more directly exposed to low-elevation coastal zones, and less likely to benefit from historically accumulated protection infrastructure.

Discussion

This study provides a globally consistent assessment of climate hazard emergence and coastal flood exposure across global cities, combining regional climate projections with harmonised urban spatial definitions. By integrating CORDEX simulations to GHS-UCDB urban polygons, we develop a globally comparable framework for assessing urban climate risks across regions, city typologies, and socio-economic contexts, with the flexibility to incorporate the next generation of CMIP6-CORDEX simulations as they become available. A central finding is the clear sequencing of hazard emergence. Temperature-related extremes (TX90p, TN90p) and cooling demand indicators emerge earliest and most universally, often before 2025 in all cities. Heat stress (HI41), drought (CDD), and fire weather (FWI) follow shortly thereafter, while precipitation extremes (RX1DAY) and energy-demand indicators display later and more heterogeneous emergence patterns. This hazard-specific timing is remarkably consistent across continents and urban typologies, indicating that physical climate signal characteristics dominate over development pathways in determining when cities cross emergence thresholds. Differences across city typologies are secondary compared to differences across hazard types. This suggests that, at the global scale, thermodynamic warming signals overwhelm variations in governance orientation or development strategy when considering emergence timing.

Typologies become more relevant when examining exposure and socio-economic gradients. The coastal flooding analysis, based on the 100 yr return period event, reveals a robust negative relationship between urban GDP and projected flooded area under the NO_PROT scenario. In the absence of protection, lower-income cities are projected to systematically experience higher proportional exposure, with particularly strong gradients in Africa and Central & South America. This indicates that physical hazard alone would likely amplify existing global inequalities in urban coastal risk. However, the maintenance of at least present levels of coastal protection standards substantially weakens or neutralizes these gradients across most continents and typologies. Under the PROT scenario, correlations between GDP and flooded fraction diminish markedly and often lose statistical significance. This demonstrates that adaptation, when implemented effectively, has the potential to reduce wealth-dependent disparities in projected exposure. At the same time, the persistence of modest correlations in some regions (e.g., Asia and Europe) indicates that protection will not fully eliminate structural inequalities. While megacities concentrate population and economic assets, the highest relative flooded fractions are predominantly observed among smaller and medium-sized coastal cities. This pattern suggests that relative spatial vulnerability may be more acute in smaller cities, which may lack extensive legacy protection systems. This finding challenges a predominantly megacity-centric framing of global climate risk. Although large metropolitan areas remain critical nodes of systemic risk, the distributional analysis highlights that proportional impacts, and potentially adaptation gaps, may be more severe in smaller urban centres. These cities may have more limited fiscal capacity, weaker governance structures, and fewer resources for large-scale coastal protection, making them particularly vulnerable to escalating sea-level rise. This finding reinforces the need to move beyond a megacity-centric perspective of climate risk and to explicitly account for small and intermediate coastal cities in global adaptation planning.

By relying on harmonised global urban polygons rather than model-based urban masks, this study circumvents the lack of consistent urban parameterisation across regional climate models. While the limitation of this approach is that it does not explicitly resolve urban canopy processes, it nevertheless ensures spatial comparability and enables a first-order global assessment of how climate extremes intersect with real urban extents. The results therefore provide a bridge between regional climate projections and city-scale risk analysis, pending the next generation of globally consistent urban-resolving simulations.
Taken together, the results indicate that (i) climate hazard emergence in cities is primarily hazard-driven and already underway for warming-related extremes, (ii) coastal flood exposure without adaptation would strongly reinforce global socio-economic disparities, and (iii) effective protection measures can substantially attenuate, but not entirely remove, these inequalities. The convergence of hazard emergence by mid-century across most continents suggests that urban adaptation planning is very urgently needed, especially given the substantial lead-times for implementation of adaptation measures. At the same time, the disproportionate relative exposure of smaller coastal cities underscores the need for inclusive, globally distributed adaptation strategies that extend beyond the world's largest metropolitan regions.

Methods

Selection of cities

City typologies, developed by Montfort et al. (2026)[33] among approximately 11,000 cities worldwide with at least 50,000 inhabitants, are derived through a data-driven Deep Embedded Clustering (DEC) ensemble approach that groups cities based on shared structural characteristics relevant for climate action, including demographic scale and growth, socio-economic development, infrastructure conditions, and biophysical energy demand patterns. Stability assessments across 30 independent clustering runs were performed to ensure robustness and reduce stochastic variability in the classification. The resulting framework identifies four city types capturing major dimensions of urban development and climate relevance: Type 1: "Development First", characterized by low emissions and urgent development challenges; Type 2: "Urban Planning First", representing rapidly growing cities supported by robust infrastructure and governance structures; Type 3: "Mitigation First", including high-emission cities with substantial mitigation potential; and Type 4: "Megacities", comprising globally significant metropolitan areas facing complex, cross-cutting socio-environmental pressures. Using this globally consistent typology enables a systematic and transparent selection of case-study cities across all AR6 regions[40], ensuring representation of diverse urban contexts rather than relying on ad hoc or literature-driven sampling. By explicitly accounting for population size and geographic distribution, the selection framework balances representativeness and societal relevance, while helping to counteract long-standing biases in the scientific literature that tend to overrepresent large cities in the Global North. Leveraging the full dataset of ~11,000 cities strengthens the generalisability of our findings and provides a structured basis for linking local climate signals to broader global urban patterns.

CORDEX-CORE climate projections

In this analysis, we use all available CORDEX-CORE regional climate model simulations at 0.22° horizontal resolution over the North American (NAM), South American (SAM), Central American (CAM), African (AFR), Australasian (AUS), Western Asian (WAS), Eastern Asian (EAS), and South-East Asian (SEA) domains, and at 0.11° resolution over the EURO-CORDEX domain (Supplementary Table 1). The simulations are driven by CMIP5 global climate models and provide continuous, daily, multi-decadal climate projections that enable a consistent multi-region and multi-city assessment of climate extremes.
Dedicated urban representations are not yet consistently available in regional climate simulations across all continents. Therefore, to ensure globally consistent spatial coverage and multi-decadal simulations across all regions, this study relies on the CORDEX-CORE CMIP5 regional climate simulations

described above. Urban centers are identified using the Global Human Settlement Urban Centre Database (GHS-UCDB, Globe R2024A[30]), which provides globally harmonised polygon geometries and associated metadata for urban areas derived from morphological built-up patterns and population-density thresholds. The list of cities considered in this study is taken from Montfort et al. (2026)[33], and the corresponding urban polygon geometries are retrieved from the GHS-UCDB database when available. This results in approximately 11,000 cities worldwide included in the analysis. For each city, the corresponding polygon is spatially overlaid with the CORDEX regional climate model grids. Climate indicators are extracted from the regional model grids and spatially aggregated over the grid cells intersecting each urban polygon. When at least five grid cells fall within the polygon, city-scale values are computed as the mean across those cells. For smaller cities intersecting fewer grid cells, a fallback approach is applied based on nearest-neighbour sampling combined with local spatial averaging, ensuring robust estimation of city-scale signals. City-level indicators are computed independently for each model simulation and subsequently combined across the multi-model ensemble. By linking gridded climate projections to standardised urban polygons, the methodology ensures spatial consistency, cross-regional comparability, and reproducibility of city-scale climate metrics.

Coastal flooding datasets

The coastal flooding analysis is based on two global coastal flood hazard datasets that represent contrasting assumptions regarding coastal protection,following the methodological frameworks of Kirezci et al. (2020)[35] (NO_PROT) and Tiggeloven et al. (2020)[38] (PROT). The NO_PROT dataset represents a counterfactual scenario in which no coastal protection measures are assumed to be in place. Coastal flood hazards are derived by combining estimates of present-day global extreme sea level (ESL) simulations with IPCC AR5 projections of relative sea-level rise (RSLR) under different climate scenarios. Extreme sea levels include the combined effects of astronomical tides, storm surge, and wave setup, and are estimated using different extreme value analyses (EVA) (adopting the best tested Peaks-over-Threshold approach with Generalized Pareto Distribution) to the time series of total sea level as the linear summation of aforementioned components tides, surge and wave setup. Future ESLs are obtained by superimposing probabilistic RSLR projections onto present-day extremes. Flood-prone areas are identified using the high-resolution Multi-Error-Removed Improved-Terrain Digital Elevation Model (MERIT DEM[41]) by using a GIS-based bathtub approach that maps areas below projected ESLs that are hydrologically connected to the ocean. Flood impacts are then quantified by overlaying inundation maps with spatially explicit datasets of population and gross domestic product (GDP), enabling the estimation of exposed assets and population. In contrast, the PROT dataset explicitly incorporates the presence of standards of coastal protection. Present-day tide and storm surge information is derived from the GTSR[42], and tropical cyclone impacts are enhanced through the inclusion of synthetic cyclone events based on the IBTrACS archive[43], improving the representation of extreme water levels in tropical regions. Extreme sea levels are modelled using a Gumbel distribution. Coastal inundation is simulated using a GIS-based bathtub methodology similar in principle to NO_PROT, but with additional refinements, including corrections for vertical datums, and attenuation of floodwaters as they propagate inland over MERIT DEM topography. Crucially, this dataset integrates spatially explicit information on coastal defence standards from the FLOPROS database[44], allowing the flood hazard to be conditioned on existing protection levels. Future hazard projections account for regional RSLR estimates from Jackson & Jevrejeva (2016) [45] under RCP4.5 and RCP8.5, combined with land subsidence projections from the SUB-CR model[46], thereby representing both climatic and geophysical drivers of relative sea-level change. Flood maps are generated for multiple return periods (2 to 100 years) and coupled with exposure and vulnerability functions to compute Expected Annual Damages (EAD), enabling an assessment of adaptation benefits under different protection strategies.

We acknowledge that a direct quantitative comparison between coastal flood projections derived from different modelling frameworks should be interpreted with caution, as such datasets may differ in terms of hydrodynamic models, digital elevation models, boundary conditions, and process representations (see Supplementary Table 2 for a detailed comparison of the two methods). In particular, the NO_PROT and PROT datasets rely on distinct methodological assumptions, including the representation of vertical land motion and coastal protection standards in PROT, which are only partially available at the global scale. Nevertheless, despite these differences, comparing the two datasets remains informative for a relative assessment of the potential role of coastal protection in modulating flood exposure. Rather than aiming at an exact inter-model attribution, our analysis focuses on contrasting flood extents under scenarios with and without protection to identify robust, first-order patterns and broad-scale tendencies across regions and city typologies. This approach allows us to place our results within the range of existing global coastal flood assessments and to highlight consistent signals that are relevant for large-scale risk interpretation, while explicitly recognizing the underlying uncertainties.

The framework of the Time of Emergence

The concept of time of emergence (ToE) is widely used across disciplines to identify the point at which a forced signal becomes distinguishable from background variability. In climate science, ToE marks the moment when the climate-change signal of a given variable exceeds the range of natural variability, allowing the influence of anthropogenic forcing to be robustly detected. This framework can be applied to a wide range of climate hazards, including temperature extremes, precipitation extremes, drought- and fire-related indices, and compound indicators. In this study, ToE is defined as the year in which the change in a given hazard index exceeds the upper bound of its internal-variability envelope. This envelope is estimated using ±2 standard deviations (σ) of the climate-model ensemble distribution over a historical reference period (1980–2010). ToE is then identified as the first year in which the 30-year running mean of the ensemble-mean hazard index crosses this threshold. This approach follows the widely adopted ±2σ detectability criterion, which approximates a 95% confidence range for internal variability[47]. By requiring the forced signal to exceed this threshold, we ensure that emergence is attributed to anthropogenic climate change rather than to fluctuations expected under natural variability alone. To assess the robustness of the ToE estimates, we complement this confidence-interval method with a signal-to-noise (S/N) analysis, in which emergence is detected once the forced change in the hazard index exceeds the simulated interannual variability. We adopt S/N > 1 as our central criterion (signal larger than noise), consistent with previous studies[7,47,48].

Declarations

Acknowledgements:

NZ, FR acknowledge the support from the European Union's HORIZON Research and Innovation Actions under grant agreement No 101081555, project IMPETUS4CHANGE. G.S.L.

RR is partly supported by the AXA Research Fund.

Author contributions: CRediT

Conceptualization: R.N., N.Z., E.C.;

Methodology: R.N., N.Z, F.R., E.C., F.C., T.M.D., R.R.;

Software: R.N, N.Z, F.R.,T.M.D.;

Formal analysis: R.N.;

Data curation: N.Z., F.C., F.R., T.M.D., R.N.;

Visualization: R.N.;

Writing - original draft: R.N.;

Writing - review & editing: R.N., N.Z., F.R.,T.M.D., R.R.,F.C.,F.R.,E.C. ;

Supervision: E.C.;

Competing Interests statement:

The authors declare no competing interests.

Data availability

The climate model data used in this study are publicly available from the Earth System Grid Federation (ESGF) data portal https://esgf-node.llnl.gov.

References

1. Pörtner, H.-O. et al. Climate change 2022: Impacts, adaptation and vulnerability. https://www.researchgate.net/profile/Vincent-Moeller/publication/362431678_Climate_Change_2022_Impacts_Adaptation_and_Vulnerability_Working_Group_II_Contribution_to_the_Sixth_Assessmen Change-2022-Impacts-Adaptation-and-Vulnerability-Working-Group-II-Contribution-to-the-Sixth-Assessment-Report-of-the-Intergovernmental-Panel-on-Climate-Change.pdf (2022).
2. Masson-Delmotte, V. et al. Summary for policymakers. Clim. Change 2021 Phys. Sci. Basis Contrib. Work. Group Sixth Assess. Rep. Intergov. Panel Clim. Change 3–32 (2023).
3. Cook, B. I., Mankin, J. S. & Anchukaitis, K. J. Climate Change and Drought: From Past to Future. Curr. Clim. Change Rep. 4, 164–179 (2018).
4. Seneviratne, S. I. et al. Weather and climate extreme events in a changing climate. Clim. Change 2021 Phys. Sci. Basis Work. Group Contrib. Sixth Assess. Rep. Intergov. Panel Clim. Change 1513–1766 (2021).
5. Dai, A. Increasing drought under global warming in observations and models. Nat. Clim. Change 3, 52–58 (2013).
6. Abatzoglou, J. T., Williams, A. P. & Barbero, R. Global Emergence of Anthropogenic Climate Change in Fire Weather Indices. Geophys. Res. Lett. 46, 326–336 (2019).
7. Nogherotto, R., Raffaele, F., Giuliani, G. & Coppola, E. Has the Fire Weather Index Emerged? Insights from Global and Regional Climate Models. Weather Clim. Extrem. 100861 (2026).
8. Fox-Kemper, B. Ocean, cryosphere and sea level change. in AGU fall meeting abstracts vol. 2021 U13B-09 (2021).
9. Dodman, D. et al. Cities, settlements and key infrastructure. https://escholarship.org/content/qt81q9s1z4/qt81q9s1z4.pdf (2023).
10. Guerreiro, S. B., Dawson, R. J., Kilsby, C., Lewis, E. & Ford, A. Future heat-waves, droughts and floods in 571 European cities. Environ. Res. Lett. 13, 034009 (2018).
11. Giorgi, F. et al. The CORDEX-CORE EXP-I initiative: description and highlight results from the initial analysis. Bull. Am. Meteorol. Soc. 103, E293–E310 (2022).
12. Coppola, E. et al. Climate hazard indices projections based on CORDEX-CORE, CMIP5 and CMIP6 ensemble. Clim. Dyn. 57, 1293–1383 (2021).
13. Ciarlo`, J. M. et al. A new spatially distributed added value index for regional climate models: the EURO-CORDEX and the CORDEX-CORE highest resolution ensembles. Clim. Dyn. 57, 1403–1424 (2021).
14. Teichmann, C. et al. Assessing mean climate change signals in the global CORDEX-CORE ensemble. Clim. Dyn. 57, 1269–1292 (2021).
15. Im, E.-S. et al. Emergence of robust anthropogenic increase of heat stress-related variables projected from CORDEX-CORE climate simulations. Clim. Dyn. 57, 1629–1644 (2021).
16. Torres-Alavez, J. A. et al. Future projections in tropical cyclone activity over multiple CORDEX domains from RegCM4 CORDEX-CORE simulations. Clim. Dyn. 57, 1507–1531 (2021).

17. Gnitou, G. T., Tan, G., Niu, R. & Nooni, I. K. Assessing past climate biases and the added value of CORDEX-CORE precipitation simulations over Africa. Remote Sens. 13, 2058 (2021).
18. Reboita, M. S. et al. Future projections of extreme precipitation climate indices over South America based on CORDEX-CORE multimodel ensemble. Atmosphere 13, 1463 (2022).
19. Argüeso, D., Evans, J. P., Fita, L. & Bormann, K. J. Temperature response to future urbanization and climate change. Clim. Dyn. 42, 2183–2199 (2014).
20. Chapman, S., Watson, J. E. M., Salazar, A., Thatcher, M. & McAlpine, C. A. The impact of urbanization and climate change on urban temperatures: a systematic review. Landsc. Ecol. 32, 1921–1935 (2017).
21. Kusaka, H., Hara, M. & Takane, Y. Urban climate projection by the WRF model at 3-km horizontal grid increment: dynamical downscaling and predicting heat stress in the 2070's August for Tokyo, Osaka, and Nagoya metropolises. [illegible] [illegible] 2 [illegible] 90, 47–63 (2012).
22. Li, D. & Bou-Zeid, E. Synergistic interactions between urban heat islands and heat waves: The impact in cities is larger than the sum of its parts. J. Appl. Meteorol. Climatol. 52, 2051–2064 (2013).
23. Ramamurthy, P. & Bou-Zeid, E. Heatwaves and urban heat islands: A comparative analysis of multiple cities. J. Geophys. Res. Atmospheres 122, 168–178 (2017).
24. Wouters, H. et al. Heat stress increase under climate change twice as large in cities as in rural areas: A study for a densely populated midlatitude maritime region. Geophys. Res. Lett. 44, 8997–9007 (2017).
25. Sharma, R., Hooyberghs, H., Lauwaet, D. & De Ridder, K. Urban Heat Island and Future Climate Change—Implications for Delhi's Heat. J. Urban Health 96, 235–251 (2019).
26. Smid, M., Russo, S., Costa, A. C., Granell, C. & Pebesma, E. Ranking European capitals by exposure to heat waves and cold waves. Urban Clim. 27, 388–402 (2019).
27. Junk, J. et al. Quantifying the effects of climate change on the urban heat Island intensity in Luxembourg—sustainable adaptation and mitigation strategies through urban design. Atmosphere 16, 462 (2025).
28. Langendijk, G. S. et al. Representation of global mega-cities and their urban heat island in CORDEX-CORE regional climate model simulations. Npj Urban Sustain. https://www.nature.com/articles/s42949-025-00325-6 (2025).
29. Zazulie, N. et al. Future projections of Climate Hazards in Urban and Rural Areas for European Cities Using Euro-CORDEX ensemble. https://www.researchsquare.com/article/rs-8368518/latest (2026).
30. Rivero, I. M. et al. GHS-UCDB R2024A-GHS urban centre database 2025. Eur. Comm. Jt. Res. Cent. JRC (2024).
31. Lu, Y.-C. & Romps, D. M. Extending the heat index. J. Appl. Meteorol. Climatol. 61, 1367–1383 (2022).
32. Di Giuseppe, F. et al. Fire Weather Index: the skill provided by the European Centre for Medium-Range Weather Forecasts ensemble prediction system. Nat. Hazards Earth Syst. Sci. 20, 2365–2378 (2020).
33. Montfort, S., Nachtigall, F., Repke, T., Binder, C. & Creutzig, F. A global typology of cities supporting coordinated climate action. https://infoscience.epfl.ch/entities/publication/ecd0f75e-e228-47d4-b055-8c125804038c (2026).
34. Vousdoukas, M. I. et al. Global probabilistic projections of extreme sea levels show intensification of coastal flood hazard. Nat. Commun. 9, 2360 (2018).
35. Kirezci, E. et al. Projections of global-scale extreme sea levels and resulting episodic coastal flooding over the 21st Century. Sci. Rep. 10, 11629 (2020).
36. Nawarat, K. et al. Coastal flood risk to European surface transport infrastructure at different global warming levels. Nat. Clim. Change 1–7 (2026).
37. Willard-Stepan, M., Gomez, N., Cardille, J. A., Galbraith, E. D. & Bennett, E. M. Assessing the exposure of buildings to long-term sea level rise across the Global South. Npj Urban Sustain. 5, 72 (2025).
38. Tiggeloven, T. et al. Global-scale benefit–cost analysis of coastal flood adaptation to different flood risk drivers using structural measures. Nat. Hazards Earth Syst. Sci. 20, 1025–1044 (2020).
39. Cattaneo, A. et al. Worldwide delineation of multi-tier city–regions. Nat. Cities 1, 469–479 (2024).
40. Iturbide, M. et al. An update of IPCC climate reference regions for subcontinental analysis of climate model data: definition and aggregated datasets. Earth Syst. Sci. Data 12, 2959–2970 (2020).
41. Takaku, J., Tadono, T., Doutsu, M., Ohgushi, F. & Kai, H. Updates of 'AW3D30'ALOS global digital surface model with other open access datasets. Int. Arch. Photogramm. Remote Sens. Spat. Inf. Sci. 43, 183–189 (2020).
42. Muis, S., Verlaan, M., Winsemius, H. C., Aerts, J. C. & Ward, P. J. A global reanalysis of storm surges and extreme sea levels. Nat. Commun. 7, 11969 (2016).
43. Knapp, K. R., Kruk, M. C., Levinson, D. H., Diamond, H. J. & Neumann, C. J. The international best track archive for climate stewardship (IBTrACS) unifying tropical cyclone data. Bull. Am. Meteorol. Soc. 91, 363–376 (2010).
44. Scussolini, P. et al. FLOPROS: an evolving global database of flood protection standards. Nat. Hazards Earth Syst. Sci. 16, 1049–1061 (2016).
45. Jackson, L. P. & Jevrejeva, S. A probabilistic approach to 21st century regional sea-level projections using RCP and High-end scenarios. Glob. Planet. Change 146, 179–189 (2016).
46. Kooi, H. & Erkens, G. Creep consolidation in land subsidence modelling; integrating geotechnical and hydrological approaches in a new MODFLOW package (SUB-CR). Proc. Int. Assoc. Hydrol. Sci. 382, 499–503 (2020).
47. Hawkins, E. & Sutton, R. Time of emergence of climate signals. Geophys. Res. Lett. 39, 2011GL050087 (2012).
48. Hawkins, E., Smith, R. S., Gregory, J. M. & Stainforth, D. A. Irreducible uncertainty in near-term climate projections. Clim. Dyn. 46, 3807–3819 (2016).

Table

***Table 1. Climate indices analysed in this study**: climate indices include temperature extremes (TN90p, TX90p), heat stress (HI41), energy-related degree days (heatDD, coolDD), precipitation extremes (CDD, RX1DAY), and fire weather conditions (FWI).*

Index	Description	Input variables	Units
TN90p	Warm nights: percentage of days when tasmin > 90th percentile of reference period (1980–2010)	tasmin	% of days
TX90p	Hot days: percentage of days when tasmax > 90th percentile of reference period (1980–2010)	tasmax	% of days
HI41	number of days with NOAA Heat Index > 41. The 'Heat Index' is a measure of how the hot weather "feels" to the human body, when relative humidity is combined with the air temperature. The Index is computed from daily relative humidity and maximum temperature, and the annual number of days with this index above a threshold of 41°C (category: danger) is provided as HI41.	tasmax, hurs	days
heatDD	Heating degree day: Describe the need for the heating energy requirements of buildings	tas, tasmax, tasmin	degree day
coolDD	Cooling degree day: Describe the need for the cooling (air-conditioning) requirements of building, used for energy consumption	tas, tasmax, tasmin	degree day
CDD	Consecutive dry days: the largest number of consecutive days where daily precipitation is below a threshold of 1 mm	pr	days
RX1DAY	Maximum 1 day precipitation	pr	mm
FWI	Fire Weather Index	tasmax, hurs, pr, sfcWind	n.a.

Figures

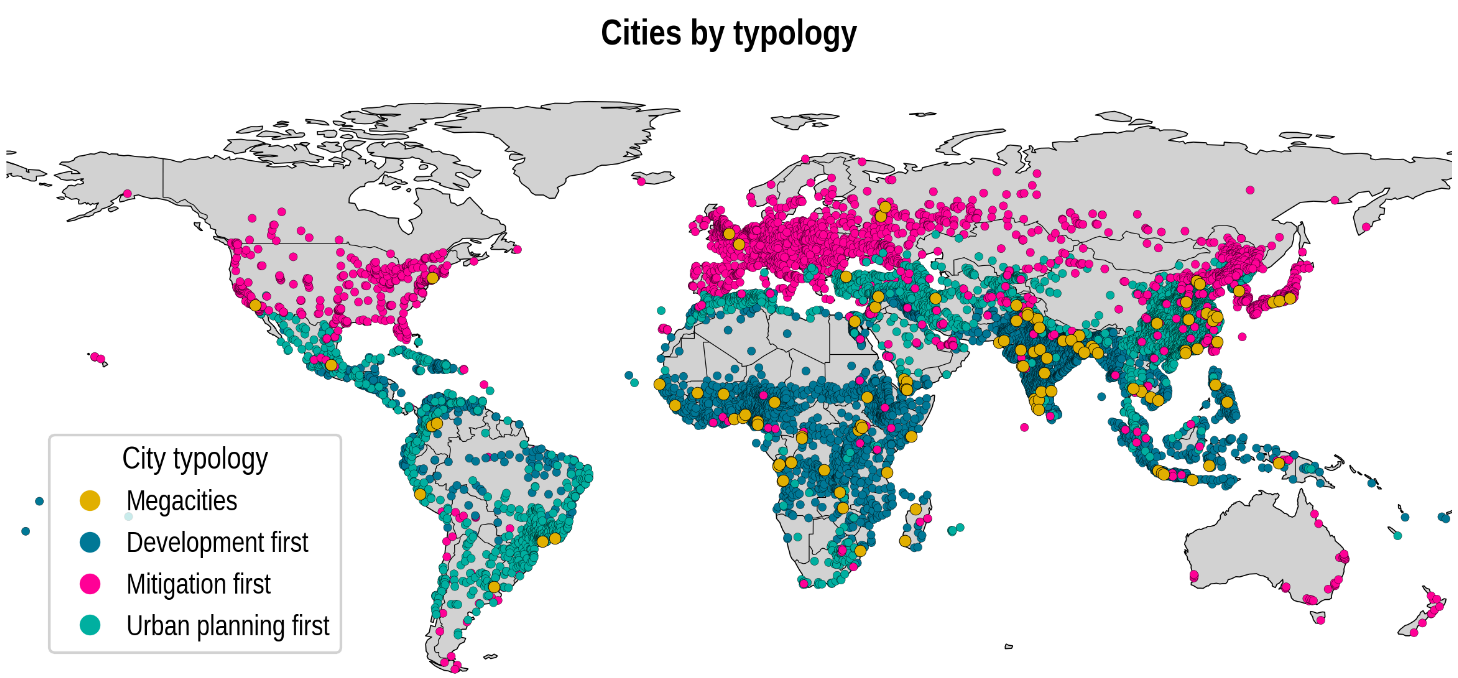

Figure 1

***Spatial distribution of cities:** ~11,000 cities analysed in this study and classified into four typologies representing different urban development priorities: Type 1: "Development First"; Type 2: "Urban Planning First"; Type 3: "Mitigation First"; and Type 4: "Megacities".*

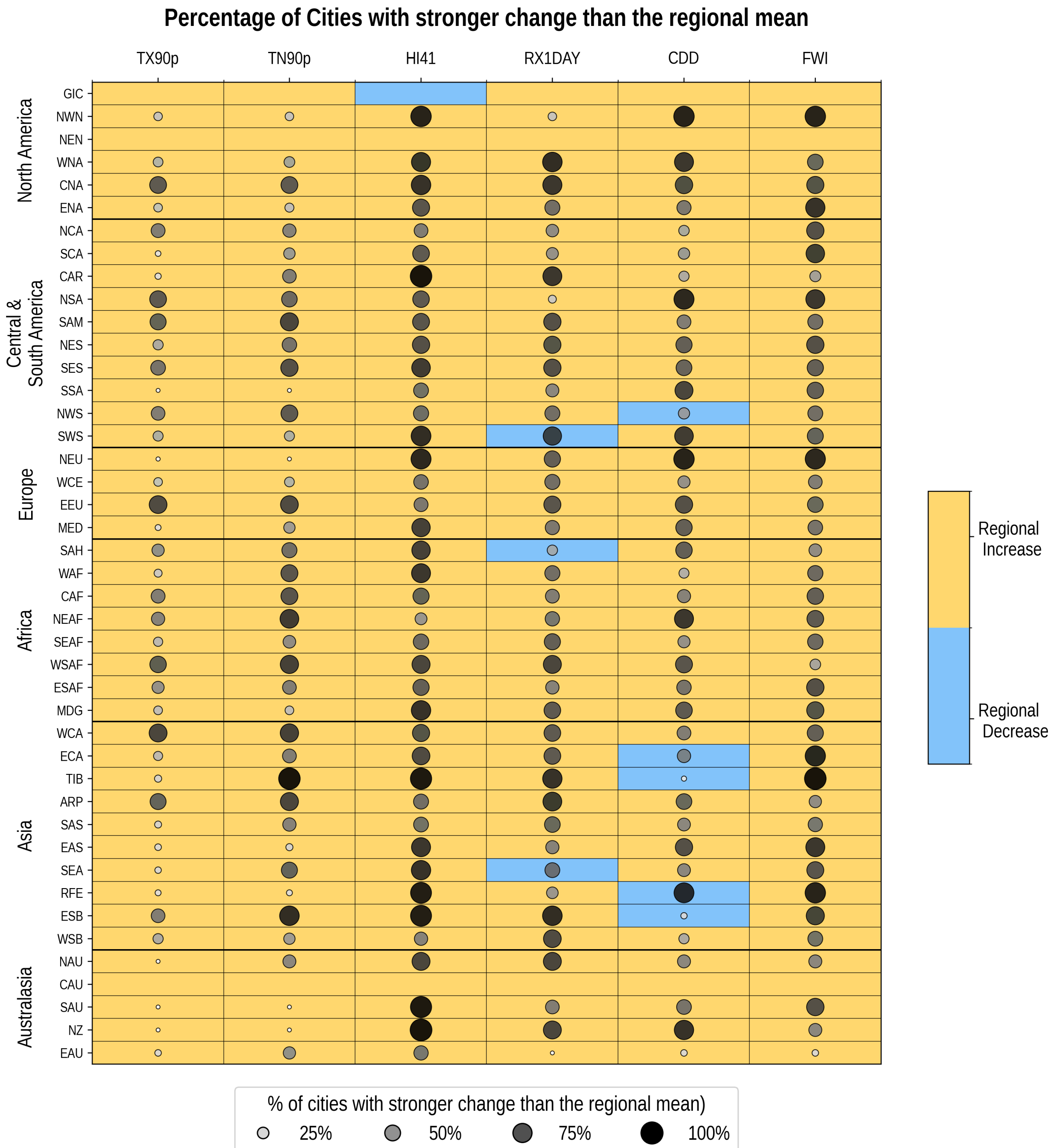

Figure 2

Percentage of cities exhibiting stronger changes than the AR6 regional mean. *Background colors indicate the sign of the regional mean change. Dots represent the percentage of cities within each AR6 region for which the magnitude of the local change exceeds the regional mean and has the same sign, i.e. sign(Δregion)·(Δcity − Δregion) > 0. Dot size and shading scale with the fraction of cities (25%, 50%, 75%, 100%). Results are based on the global dataset of ~11,000 cities and the full CORDEX-CORE ensemble. Empty cells are cells that include only one city.*

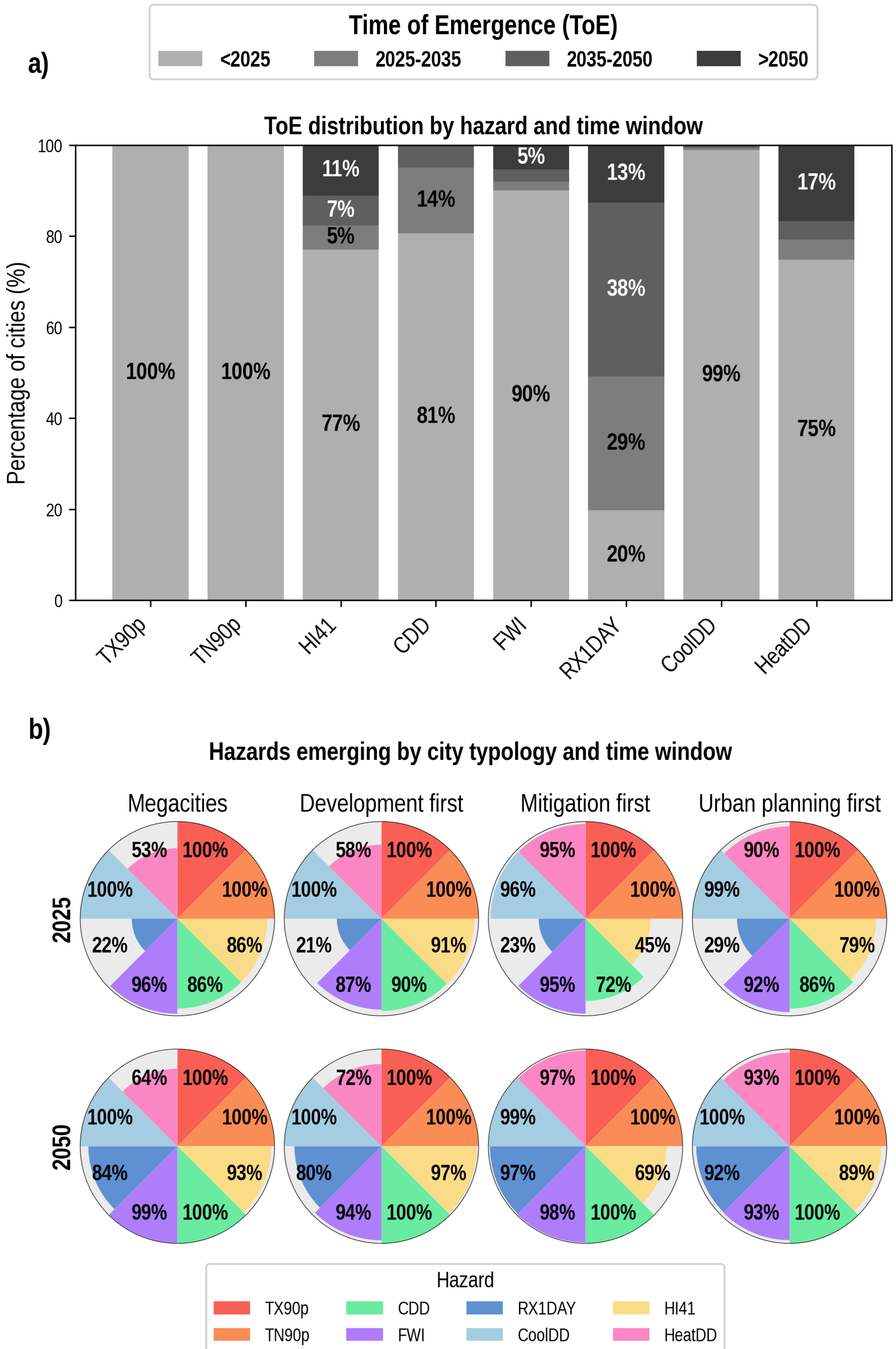

Figure 3

Time of emergence of climate hazards across cities and urban typologies. *(a) Distribution of the time of emergence (ToE) of eight climate hazards across all analysed cities, grouped into four time windows (<2025, 2025–2035, 2035–2050, >2050). Bars show the percentage of cities for which each hazard emerges within a given time window. (b) Relative contribution of different hazards emerging in two periods (2000–2025 and 2025–2050) for each city typology (development first, megacities, mitigation first, urban planning first). Pie charts indicate the proportion of hazards associated with each city typology, highlighting shifts in dominant climate risks over time and differences in emergence patterns across urban development pathways.*

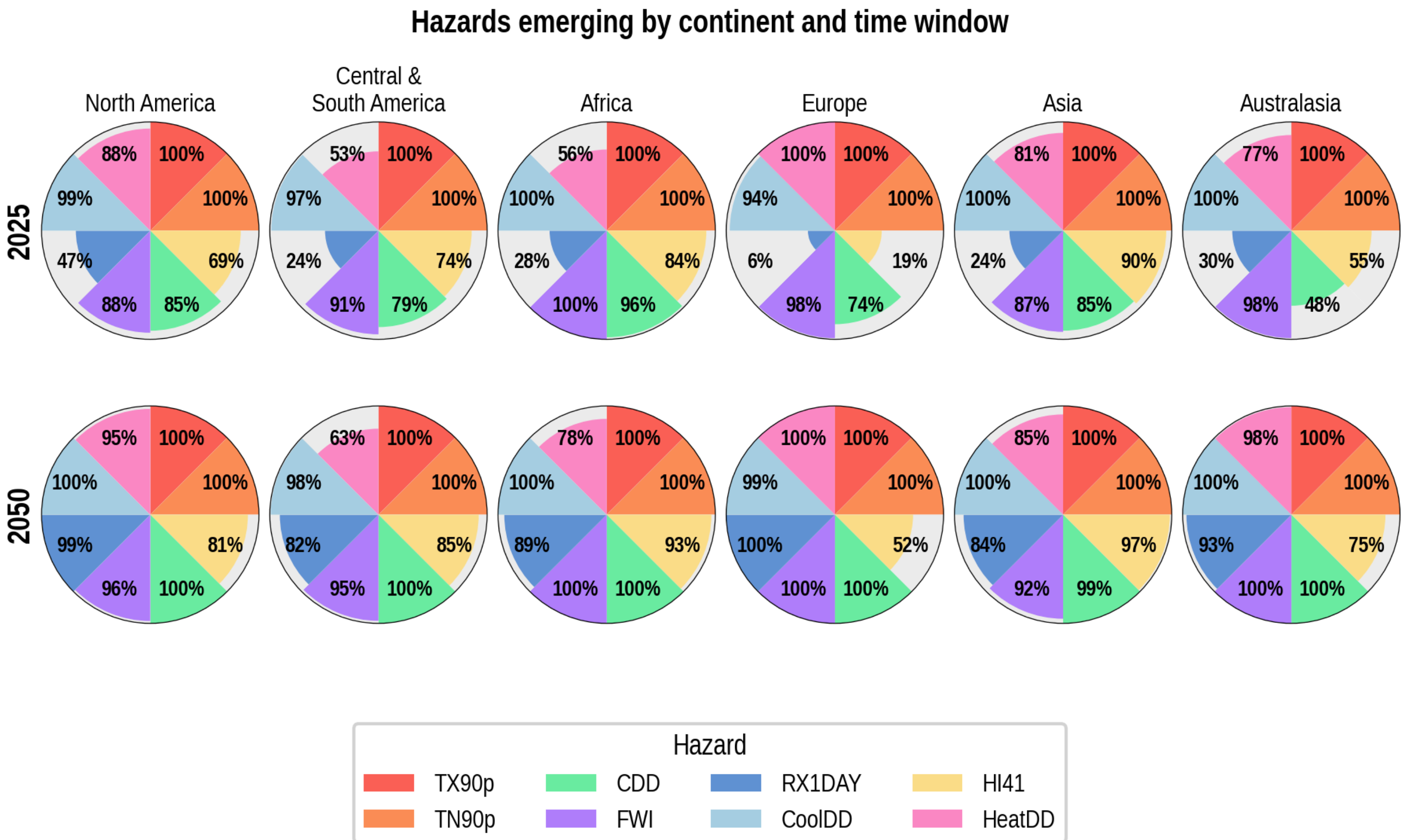

Figure 4

Time of emergence of climate hazards across cities and regions. *Continental distribution of emerging climate hazards across time windows. Pie charts show the relative composition of climate hazards emerging in two time periods (2000–2025, top row; 2025–2050, bottom row) for cities grouped by continent.*

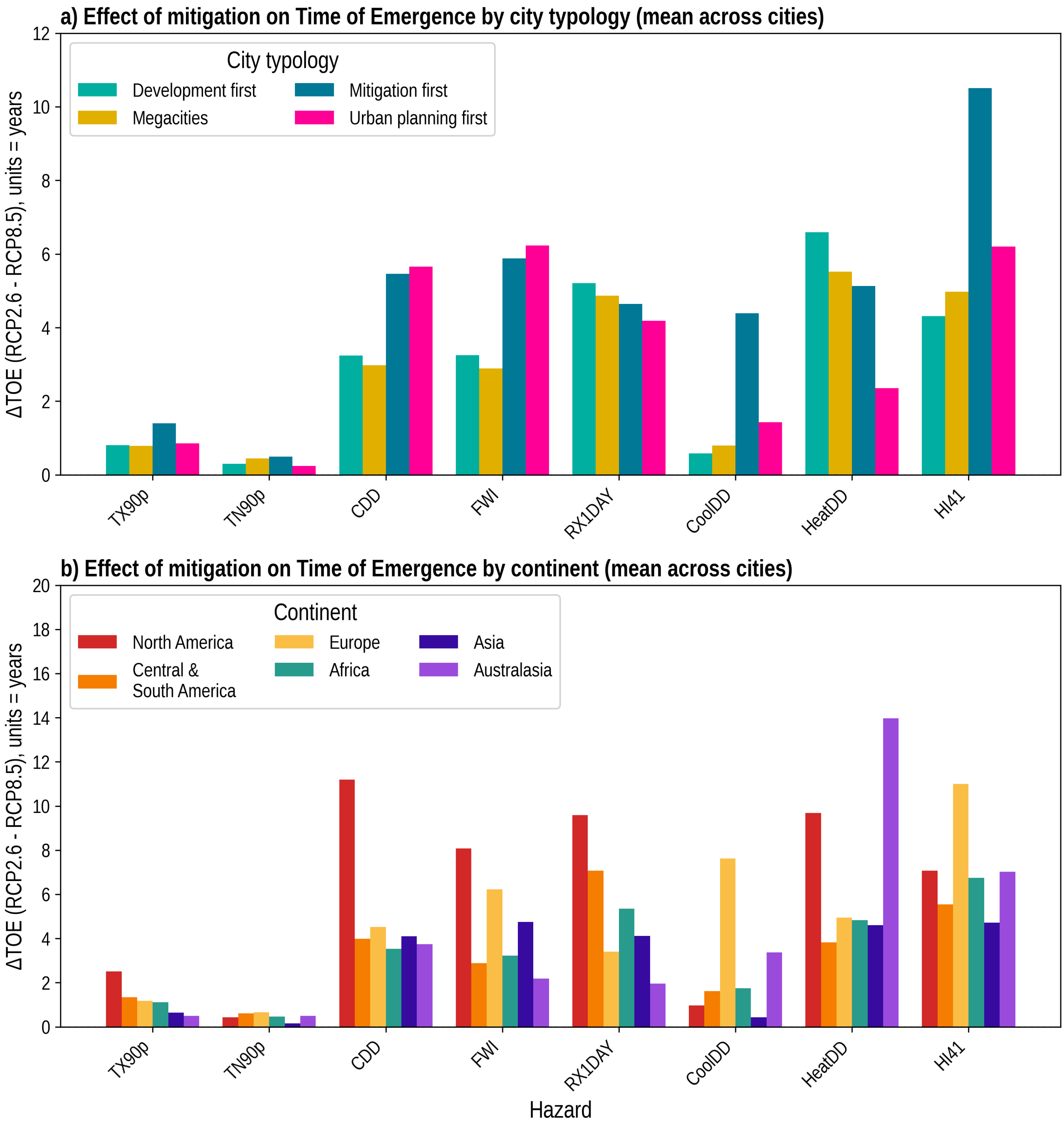

Figure 5

Effect of mitigation on the time of emergence of climate hazards across city typologies and continents*. Bars show the median delay in the time of emergence (ΔToE, years) between a low-emissions scenario (RCP2.6) and a high-emissions scenario (RCP8.5), computed across cities for each hazard. (a) shows results aggregated by city typology, while the (b) shows the same metric aggregated by continent*

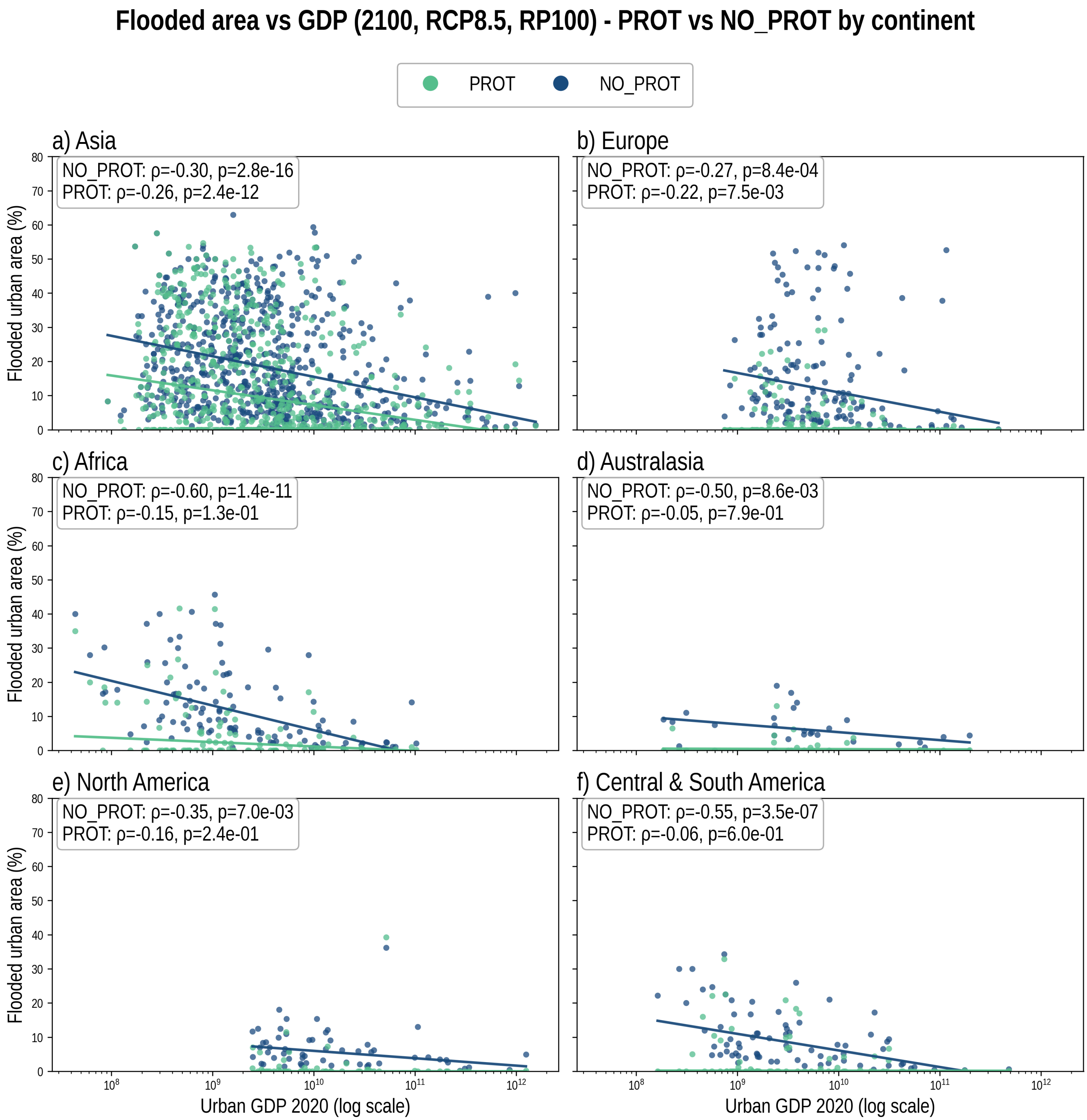

Figure 6

Flooded areas vs GDP across regions. *Relationship between flooded urban area and urban GDP across cities in different continents under a high-end climate scenario (2100, RCP8.5, 100-year return period)*

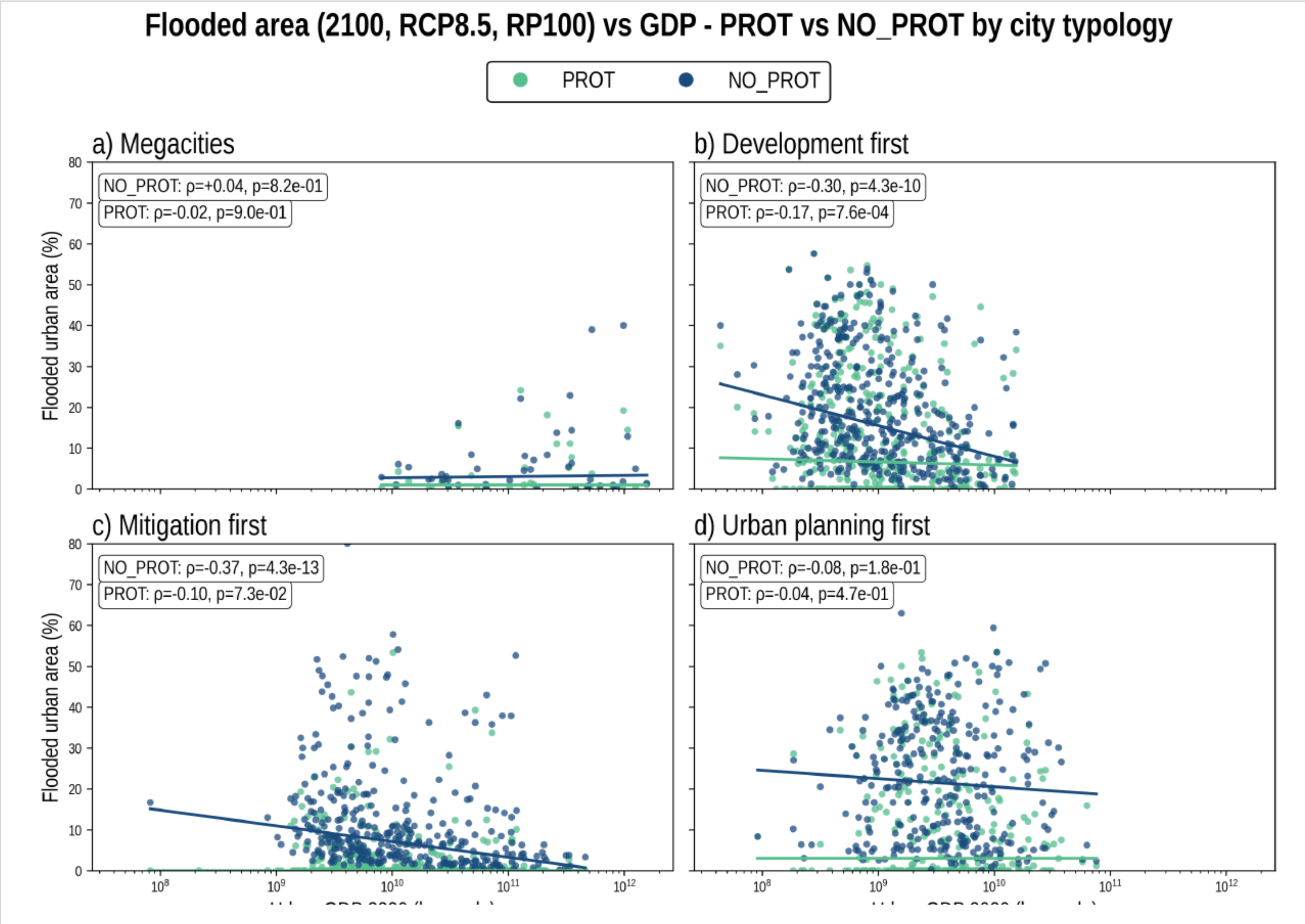

Figure 7

Flooded areas vs GDP across city types. *Relationship between flooded urban area and urban GDP across different city development typologies under a high-end climate scenario (2100, RCP8.5, 100-year return period)*

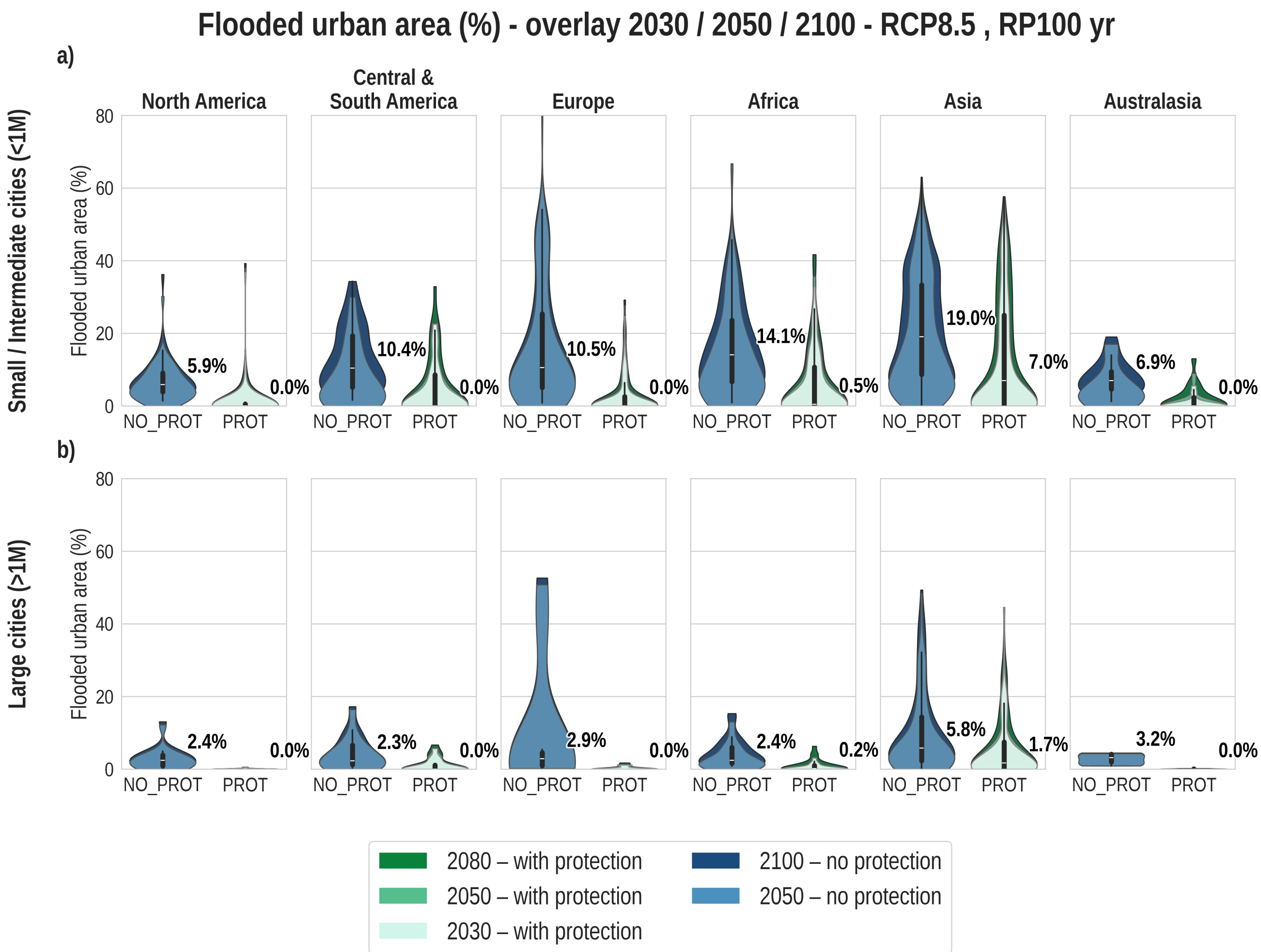

Figure 8

Flooded areas vs Population. *Flooded urban area (% of built-up land) for small/intermediate coastal cities (a), and for large cities (167 cities with >1M inhabitants, (b)) under a 100-year return-period coastal flood event (RCP8.5), for 2030/2050/2100 and with vs. without coastal protection. Violin plots show the distribution across cities grouped by continent, with the median value annotated.*

Supplementary Files

This is a list of supplementary files associated with this preprint. Click to download.

- SUPPMATERIAL.docx